Transport in Porous Media
https://doi.org/10.1007/s11242-018-1189-9

Effects of Image Resolution on Sandstone Porosity and Permeability as Obtained from X-Ray Microscopy

Kelly M. Guan[1] · Marfa Nazarova[2,3] · Bo Guo[1] · Hamdi Tchelepi[1] · Anthony R. Kovscek[1] · Patrice Creux[1,2]

Received: 29 June 2018 / Accepted: 29 October 2018

Abstract
Estimating porosity and permeability for porous rock is a vital component of reservoir engineering, and imaging techniques have to date focused on methodologies to match image-derived flow parameters with experimentally identified values. Less emphasis has been placed on the trade-off between imaging complexity, computational time, and error in identifying porosity and permeability. Here, the effect of image resolution on the permeability derived from micro-X-ray microscopy (micro-XRM) is discussed. A minicore plug of Bentheimer sandstone is imaged at a resolution of $1024 \times 1024 \times 1024$ voxels, with a voxel size of $1.53\,\mu$m, and progressively rebinned to as low as 32 voxels per side (voxel size $48.96\,\mu$m). Pore-scale flow is modeled using the finite volume method in the open-source program OpenFOAM®. A sharp drop in permeability between images with a voxel size of 24 and $12\,\mu$m suggests that an optimal speed/resolution trade-off may be found. The primary source of error is due to reassignment of voxels along the pore–solid interface and the subsequent change in pore connectivity. We observe the error in permeability and porosity due to both image resolution and thresholding values in order to find a method that balances an acceptable error range with reasonable computation time.

Keywords Computed micro-x-ray microscopy · Microporosity · Permeability · Digital rock physics

1 Introduction

Understanding fluid flow in porous media is relevant to many fields, such as oil and gas recovery, geothermal energy, and geological CO_2 storage. Conventional methods to model

✉ Kelly M. Guan
kmguan@stanford.edu

1 Energy Resources Engineering, Stanford University, 367 Panama St., Stanford, CA 94305, USA

2 CNRS/TOTAL/UNIV PAU & PAYS ADOUR, Laboratoire des Fluides Complexes et leurs Réservoirs IPRA, UMR5150, 64000 Pau, France

3 Centre Scientifique et Technique Jean Féger (CSTJF), TOTAL Exploration and Production, Avenue de Larribau, 64000 Pau, France

fluid flow in reservoirs often assume a simplified pore geometry that is not representative of the actual rock structure. Digital rock physics (DRP) is a research area that focuses on the imaging and digitization of pore and mineral phases in rocks to use as an input in numerical simulations. These simulations capture the physics behind different rock processes, such as fluid transport, elastic deformation, and electrical current flow (Andrä et al. 2013a, b). Improvements in imaging techniques, namely micro-x-ray microscopy, allow for the 3D reconstruction of rock volumes at resolutions that often resolve most of the pore space, depending on the rock type (Wildenschild and Sheppard 2013). For sandstones that are isotropic and smooth, such as Berea or Fontainebleau, imaging and segmentation is a relatively straightforward step given a sufficient voxel size (Schlüter et al. 2014).

Medical CT scanning has been widely used for 3D imaging of core-sized samples. The quick scan time, coupled with a stationary sample setup, has made it suitable for observing single and multiphase flow in intact cores (Aljamaan et al. 2013; Vega et al. 2014; Vinegar and Wellington 1987). Typical X-ray energies range from 80 to 140 keV, and spatial resolutions are on the 100 μm length scale. As CT technology has evolved, greater resolution scans have been achieved using more powerful sources and different scan geometries. Synchrotron-based micro-XRM may produce scans with 10 s nm voxel sizes. Restrictions on sample size and limited access to facilities, however, make it difficult to use for regular characterization purposes. Laboratory- or industrial-scale micro-XRM is more accessible and provides spatial resolutions on the micrometer scale for sample sizes ranging from hundreds of micrometers to tens of centimeters (Cnudde and Boone 2013). Many types of quantitative information are obtained from micro-XRM data such as porosity and grain size, material texture, component volume fractions, and pore connectivity. Pore networks can be extracted from these scans in order to calculate petrophysical properties, usually porosity and permeability. Other relevant properties, such as relative permeability and capillary pressure, may also be investigated but, due to their more complex derivations, may require additional measurements or higher-resolution imaging techniques to yield reliable estimates. Nonetheless, porosity and permeability are among the most important petrophysical properties obtained from image-based methods for evaluating porous media flow.

One important parameter when considering image resolution and quality is the signal-to-noise ratio (SNR). The signal-to-noise ratio is a function of frame rate, acquisition time, and number of pixels binned. A high-resolution image will often suffer from poor SNR due to the number of bins. Increasing the frame rate and acquisition level can improve the quality, but leads to long acquisition times and large file sizes. To address this, researchers will often acquire the image at a lower resolution or rebin the pixels during the post-processing step (Shah et al. 2016). Low-resolution images may have less noise, but suffer from blurring at the interface between the pore space and solid.

During the post-processing step, filters such as bilateral, non-local means, and Gaussian kernel methods are used to reduce noise while preserving edge features (Schlüter et al. 2014; Kaestner et al. 2008). The choice of filter also influences the image segmentation step. Many techniques are available: Simple, classic ones such as Otsu's method minimizes the within class variance between features, while others such as the watershed method measure the local gradient around an area to classify pixels. The simplest method, histogram-based thresholding, enables the observer to inspect visually the accuracy of the binarized image over the original rock image. This method truncates the tail of the distribution for each class and can lead to misclassification of pixels near the edges. Depending on the input image quality, choice of filter, and segmentation method, the resulting binary pore and solid network can vary considerably (Sheppard et al. 2004).

Many researchers have studied the effect of image quality and processing, sampling volume, and model parameters on rock properties derived from DRP. Some have used pore network (PN) models, which extract pore and throat networks from 3D images, for modeling (Beckingham et al. 2013; Shah et al. 2016). One disadvantage to this method is that the pore network represents an approximation of the actual pore structure. Others used the fully resolved pore space to directly model the flow pathway, usually using a lattice Boltzmann (LB) or Stokes method (Leu et al. 2014; Peng et al. 2014; Guibert et al. 2015; Shah et al. 2016; Soulaine et al. 2016; Saxena et al. 2018). Image resolution affects many steps in the image processing and modeling pipeline. For PN modeling, changes in image resolution may lead to different extracted pore networks and therefore changes in permeability (Beckingham et al. 2013). In LB methods, researchers have also shown that image resolution and other parameters such as thresholding choice and field of view affect the range of acceptable porosity and permeability values (Leu et al. 2014; Peng et al. 2014; Saxena et al. 2018).

Understanding the range of error due to image quality and resolution, and its effect on pore connectivity, has not been extensively studied (Bazaikin et al. 2017). In order to do so, a clear methodology and simple approach is necessary. Workflows have been proposed for generating ground-truth-type images for comparison, but implementation to estimate flow properties has yet to be done (Berg et al. 2018). The main contribution of this work lies in describing and implementing a methodology for estimating errors in image-based calculations of porosity and permeability.

To proceed, Sect. 2 presents the experimental (image processing, characterization) and numerical work flows. Then, the results of the imaging and numerical modeling techniques are presented in Sect. 3: changes in the estimated values of porosity and permeability due to rebinning of the input image, and the output and convergence of the numerical model are discussed.

2 Methods

The sample studied is a minicore plug of a Bentheimer sandstone. The plug used for imaging is 1 cm long and 3 mm in diameter. Porosity measurements on a larger plug (6 mm long, 8 mm in diameter) from the same outcrop also were also taken.

2.1 Porosimetry

Pore throat sizes and their distributions were measured using mercury intrusion porosimetry (MIP) by filling the sample with mercury up to a pressure of 33,000 psi (Micromeritics AutoPore IV 9500). Throat sizes are calculated according to the Washburn equation, and at 33,000 psi, pores down to 6.5 nm can be filled (Washburn 1921).

The bulk volume and grain density were also measured using He pycnometry (Micromeritics AccuPyc 1340). The volume of helium displaced by a solid matrix was measured for 999 cycles and then divided by sample weight to obtain the matrix grain density. The total sample porosity is determined from the difference between ρ_{bulk}, the bulk density measured by MIP, and ρ_{grain}, the grain density obtained from He pycnometry:

$$\phi = \frac{\rho_{\text{grain}} - \rho_{\text{bulk}}}{\rho_{\text{grain}}} \times 100\%. \tag{1}$$

2.2 Image Acquisition and Pixel Binning

X-ray tomographic slices were acquired using a ZEISS Xradia 520 Versa X-ray microscope. The sample was mounted onto a pin holder using epoxy and imaged using a 20X objective lens at 80 kVp. Low-energy (LE) filters were applied to increase the average beam energy and improve the transmission of X-rays through the sample. The voxel size is 1.53 µm and is determined by the objective lens strength and relative position of the source, sample, and detector. At least 1000 2D projections were collected with an exposure time of 1 second per projection as the sample was rotated 360° along the z-axis. The 2D dataset was corrected for beam hardening artifacts and reconstructed using the filtered back-projection method on XMReconstructor (Zeiss). All further image processing was performed using Avizo 9.0 (FEI).

The entire dataset collected represents a cylindrical volume 3 mm in diameter and length. A 1024 × 1024 × 1024 voxel region ($1.56 \times 1.56 \times 1.56\,\text{mm}^3$) was cropped from the center of the sample. A 3D bilateral filter was then applied to reduce image noise. Next, various thresholding ranges were selected to segment the pore space from the grains. The threshold values were chosen across a range of grayscale levels that fell in between the pore and solid phases. The product is a binary image that will be used as the input pore network for the numerical calculations.

The resolution was successfully decreased by performing pixel binning across the initial pore network. The binning method simulates the process of combining charge from adjacent pixels in a CCD during readout. This is performed prior to digitization in the on-chip circuitry of the CCD by control of the serial and parallel registers. The two main advantages of the detector binning method are to improve the signal-to-noise ratio (SNR) and increase the frame rate. However, the spatial resolution decreases as the binning amount increases. Using a high-resolution original scan is important in order to reduce noise before the rebinning process.

In this study, the binning is performed in the post-processing step so that image noise is already minimized and constant across different resolutions. From the 1024 × 1024 × 1024 voxel dataset, subsequent datasets were rebinned by a factor of 2 down to 32 × 32 × 32 voxels per side. Each step takes the average of a cube of 8 adjacent pixels from the previous level to generate the lower level. The rebinning process may also use non-integer values if the original image resolution is close to the limit of acceptable resolution. There are five rebinned samples of 512, 256, 128, 64, and 32 voxels per side (voxel size of 3.06, 6.12, 12.24, 24.48, and 48.96 µm, respectively). The images were then thresholded using the same gray-level value (Fig. 1). This value was chosen as it led to the smallest difference in porosity across the rebinned datasets (Fig. 4).

The datasets were compared in terms of changes in pore network topology in order to understand how the flow path changes during permeability calculations later. This can be expressed as the unconformity between the binned and the original dataset after binarization. The unconformity ratio (U.R.) is calculated as:

$$U.R. = \frac{\sum \mathrm{PNP}_{i,j,k,1024} \bigoplus \mathrm{PNP}_{i,j,k,nB}}{\sum \mathrm{PNP}_{i,j,k,1024}}, \tag{2}$$

where PNP is a porous network pixel at i, j, k coordinates for the binning level B. The binned images form a periodic structure of $n \times n \times n$ voxels and are compared using an exclusive-or operation with the original 1024 × 1024 × 1024 voxel dataset. The image representation of the unconformity at subsequent binning levels is shown in Fig. 1c. Voxels that change classification, from pore to solid or vice versa, after binning yield a true value and are shown

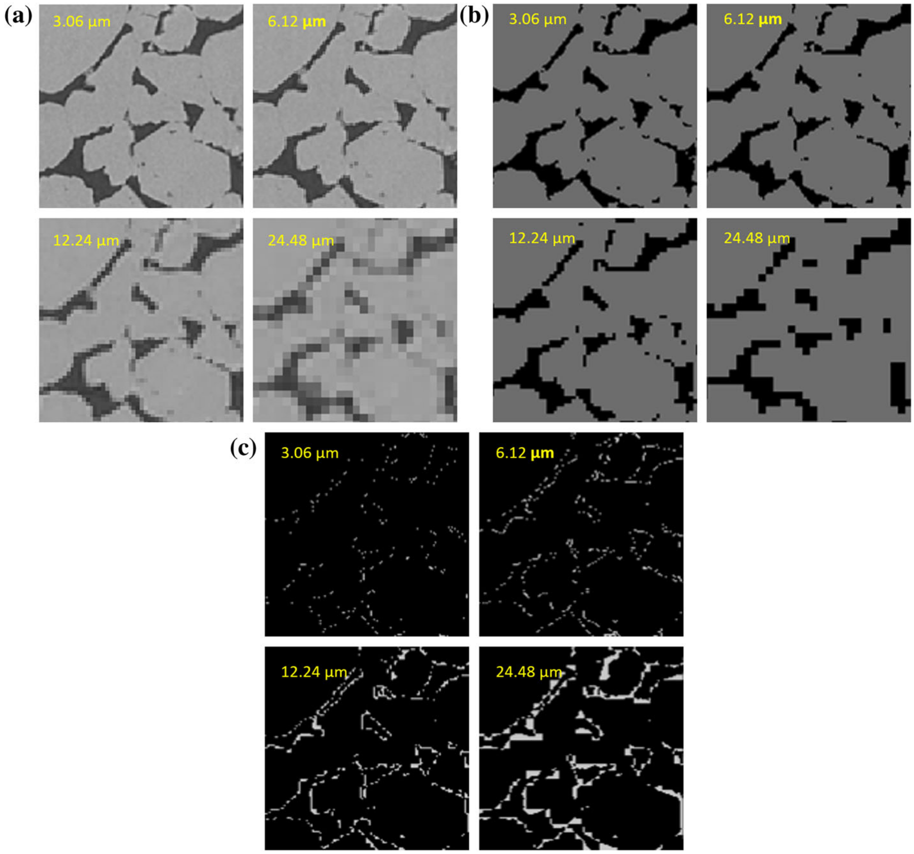

Fig. 1 2D slices represented as **a** grayscale, **b** binarized (black = pore, gray = solid), and **c** unconformity (white) across binned datasets. Voxel size for each dataset is shown in yellow. Field of view of each slice is approximately 650 µm

as white pixels. A large unconformity ratio indicates greater differences in the pore network topology between the original high-resolution image and the binned dataset. As binning occurs, the extent of dilation and/or erosion along the pore/solid interface can be evaluated through the unconformity ratio.

Finally, the changes in pore network connectivity were studied by skeletonizing the binarized images and analyzing them using the *Skeletonize3D* and *AnalyzeSkeleton* plug-ins, respectively, in ImageJ (Schneider et al. 2012; Arganda-Carreras et al. 2010). The plug-in tags each voxel as an end point (less than 2 neighbors), junction (more than 2 neighbors), or slab (exactly 2 neighbors) and then determines the number of branches and junctions and their average and maximum lengths. The largest skeleton represents the fully connected pore network, and its information is reported here. Smaller skeletons identified represent unconnected pore spaces and do not affect ultimate flow properties.

2.3 Numerical Modeling

Single-phase flow in porous media can be described by the Stokes equation at the pore scale (Bear 1972). For steady state, incompressible flow and assuming no gravity effects, the conservation and momentum equations are:

$$\nabla \cdot \mathbf{u} = 0, \tag{3}$$

$$\mu \Delta \mathbf{u} = \nabla p, \tag{4}$$

where $\mathbf{u}$ is the velocity field at each grid cell, ∇p is the pressure gradient, and μ is the dynamic viscosity. At the macroscale, this is rewritten as Darcy's law to calculate the permeability of the whole system (Whitaker 1986). The z component of the permeability tensor can be written as:

$$k_z = \frac{\mu Q}{A_{xy} \Delta p / L_z}, \tag{5}$$

where Q is the volumetric flux across a slice with area A_{xy}.

The binarized rock surface is used as the input for numerical calculations of permeability. In order to reduce the number of grid cells in the final mesh, the unconnected pore faces along the chosen flow direction (z) are removed. These unconnected pores do not contribute to flow or impact the final solution. The surface is kept as a hexahedral shape and contains an equal number of voxels in the x and y directions. In the z direction, a single-voxel layer classified as pore space is added at each end in order to maintain uniform boundary conditions at the inlet and outlet. A periodic array of the sample is considered in order to mimic conditions within a larger volume, and a body force in the form of a pressure gradient is imposed along the negative z direction. The remaining faces have a no-slip boundary condition.

To generate the mesh for the pore space, the *snappyHexMesh* utility is used from the OpenFOAM toolbox. OpenFOAM is an open-source toolbox that uses a finite volume method for direct numerical simulations (Weller et al. 1998). The *snappyHexMesh* utility generates a 3D hexahedral mesh of the pore space on top of a background mesh, generated from the *blockMesh* utility, through cell splitting and removal processes; further details can be found in the user guide (Greenshields 2015). The *simpleCycFoam* solver uses a Semi-Implicit Method for Pressure Linked Equations (SIMPLE) algorithm to solve the steady-state Stokes equation with cyclic boundary conditions (Patankar 1980).

The main adjusted parameters are transport properties and grid cell size. The kinematic viscosity is set to $1 \times 10^{-5}\,\mathrm{m^2/s}$, and the flow is driven by a body force of $100\,\mathrm{m/s^2}$. The simulation is run until convergence is reached, using a tolerance of 1×10^{-8} for p and u. The resulting output is the velocity vector and pressure in each grid cell. The 3D result is analyzed using the open-source software ParaView. The integrated velocity field is calculated at three different 2D slices along the z direction and used in Eq. 5 to determine the permeability (Fig. 2). The permeability at three different slices is averaged to yield a single value.

3 Results and Discussion

3.1 Change in Porosity and Permeability

Figures 3a and 4 show the gray-level histograms and porosity calculated at different thresholding values for the sample with a voxel size of 1.53, 3.06, 6.12, 12.24, and 24.48 µm. The experimental porosity calculated from He pycnometry and MIP was 21.84%. From the pore throat size distribution obtained from MIP, the median pore size is 34 µm (Fig. 3b). The 48.96 µm voxel size case is not shown because at this scale the voxel size approaches the pore throat size and pore connectivity is lost across the sample. Therefore, this case is not expected to be very representative of the sample at low imaging resolutions. The main

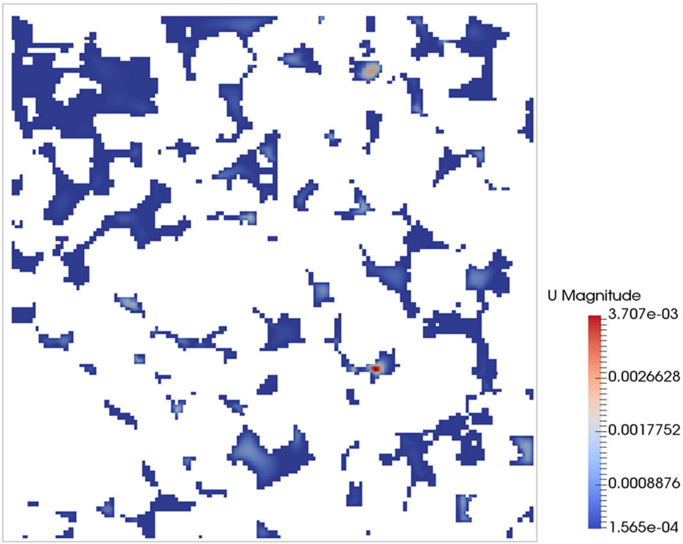

Fig. 2 2D slice of the velocity field in the XY plane, 128 voxel case

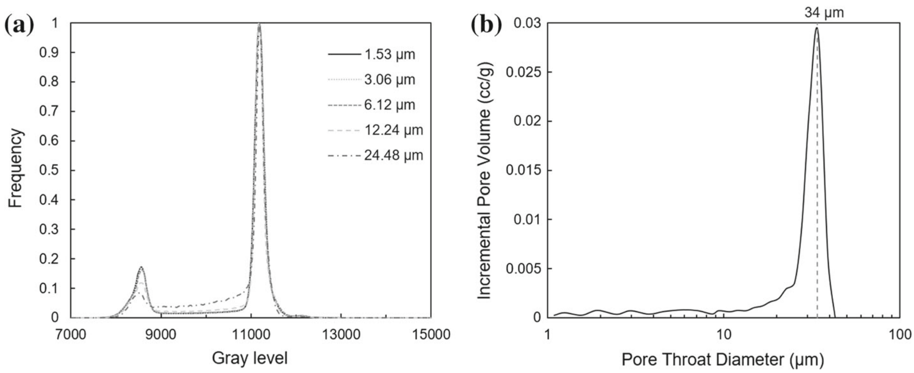

Fig. 3 **a** Frequency histogram of gray-level values for the original (1.53 μm) and binned datasets and **b** pore throat size distribution obtained from mercury intrusion porosimetry

difference in histogram shape across the binned samples is the increase in gray-level values from 9,000 to 10,000. This region corresponds to the tail ends of the pore (low attenuation and gray-level value) and solid (high attenuation and gray-level value) distributions. A histogram-based thresholding method may misclassify voxels in this region, and the effect of image degradation is apparent in Fig. 1c.

Figure 4 shows the change in porosity as a function of histogram threshold level. The behavior is roughly linear for small voxel sizes (1.53, 3.06, and 6.12 μm). The slopes of the porosity vs. gray-level lines can represent the fraction of voxels along the pore–solid interface. As voxel size increases, the slope increases due to the loss of features and importance of partial volume effects from each voxel.

Figure 5 shows the permeability and porosity as a function of voxel size. The porosity and permeability were calculated from the binarized image thresholded at a gray level of 10,000

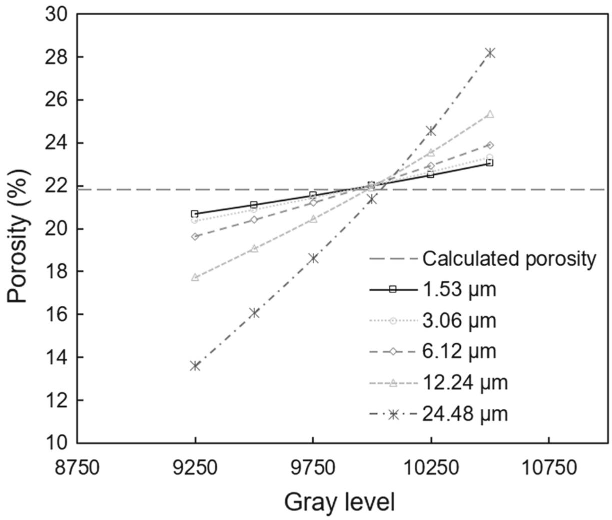

Fig. 4 Porosity versus gray-level threshold value for original and binned datasets. The experimentally derived porosity is marked along the horizontal dashed line

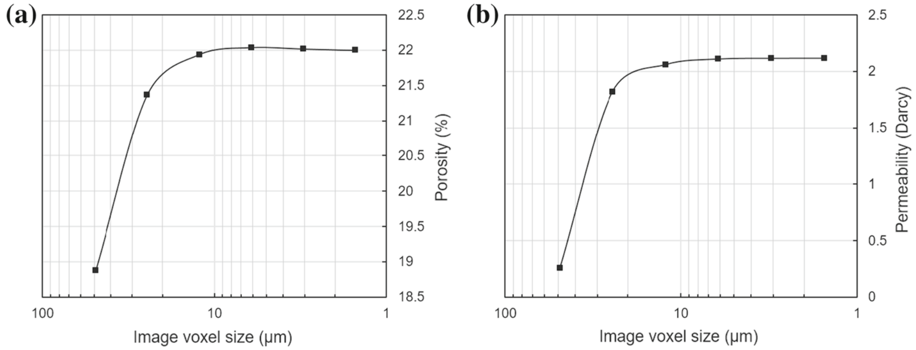

Fig. 5 **a** Porosity and **b** permeability versus sample voxel size

(see Fig. 4). At this gray-level threshold, the porosity approaches a value of 22.00% and is comparable to the experimental value of 21.84%. For this sandstone, using an automatic method such as Otsu's algorithm to threshold the grayscale histogram yields a porosity of 21.64%, which is a $< 2\%$ difference between the manual thresholding value. For well-resolved systems with a unimodal pore distribution such as this sample, the segmentation method will not affect the porosity by a large amount. For more complex rock types or when imaging at lower resolutions, choice of segmentation method may matter.

The number of grid cells used to mesh the pore space depends on the voxel size. The convergence as a function of mesh size is explored in the next section, but it is expected that a finer mesh generates a more accurate result at the cost of computation time. Therefore, the reported permeability values in Fig. 5a correspond to the finest mesh for each voxel size. The permeability increases as voxel size decreases, indicating that smaller pore pathways become more resolved and contribute to flow within the media. The value begins to converge at a voxel size of 12.24 μm and reaches a converged value of 2.12 Darcy.

Table 1 Unconformity calculated from binarized image, and number of branches, junctions, and average branch length calculated from skeletonized, binarized images

Voxels per side	Voxel size (µm)	Unconformity (%)	# Branches	# Junctions	Avg. branch length (µm)
1024	1.53	–	153,507	80,350	18.59
512	3.06	1.22	69,254	31,248	29.31
256	6.12	2.61	21,240	9486	56.35
128	12.24	5.05	6517	3060	85.79
64	24.48	8.99	2283	927	137.70

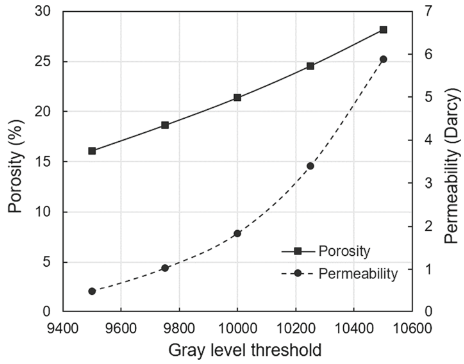

Fig. 6 Porosity and permeability as a function of gray-level threshold value for the 24.48 μm voxel size case

Table 1 shows the unconformity and the number of branches, junctions, and average branch length reported using the *AnalyzeSkeleton* plug-in. The unconformity, which was calculated in reference to the original, binarized 1024 × 1024 × 1024 voxel image, increases with voxel size due to the averaging effect at the pore/surface interface as subsampling occurs. Porosity and permeability converge for cases with an unconformity value of less than 5% for this sandstone. For the skeletonized images, the number of branches and junctions decreases with voxel size due to the inability to resolve smaller pore pathways in subsampled images. This also explains the increase in the average branch length and indicates the effect of voxel size on pore connectivity within the sample.

Figure 6 shows the relationship between porosity and permeability versus the gray-level threshold value for binarizing the 24.48 μm voxel size case. Porosity ranges from 16 to 28%, and permeability ranges from 0.5 to 5.9 Darcy. The large range of values is expected due to the large voxel size, as it is comparable to the median pore throat size (34 μm) and is more sensitive to changes in thresholding. Even though the calculated permeability at a gray level of 10,000 is close to the converged value of 2.1 Darcy, the error range due to thresholding choice becomes significant for this resolution level.

3.2 Mesh Refinement

Mesh refinement and smoothing are important parameters that affect the error and final value (Guibert et al. 2015). This study focuses on isolating the effect of image voxel resolution and thresholding error on the final permeability, so smoothing operations are not performed. For mesh refinement, the background grid cells are refined until the permeability converges. The volumetric flow rate (m^3/s) should be the same, within machine precision, along the entire z direction. The convergence may be toward an experimentally derived permeability value or until the greater refinements does not lead to significant changes in value. Here, the refinement was performed until the permeability reached the converged value of 2.11 Darcy.

Because reported permeability values and convergence are also affected by the ratio of grid cells to voxels per side, a more careful study of convergence has been done. The effect of mesh refinement was studied at two different voxel sizes, 6.12 μm and 12.24 μm. These voxel sizes are below the average throat diameter (34 μm) and make up more than 99.84 % of the total pore volume.

It is often recommended that the pore throat size is 10 times the size of a single grid cell (Saxena et al. 2018). This corresponds to a grid cell size of 3.5 μm if the median pore throat size is used. As shown in Fig. 7a, the permeability converges to a value between 2 and 2.15

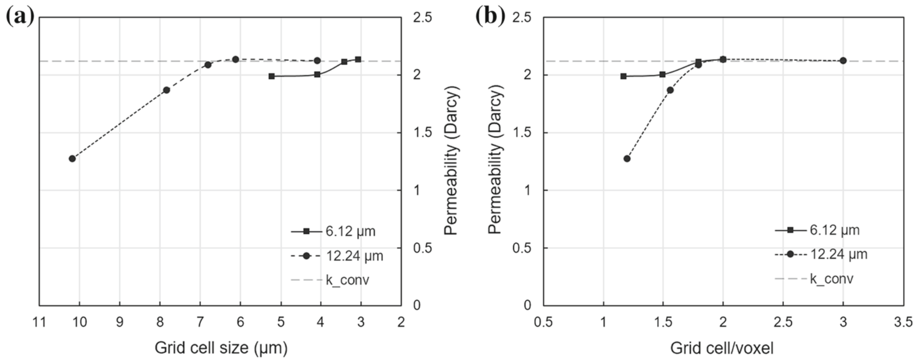

Fig. 7 Permeability as a function of **a** grid cell size and **b** number of grid cells per voxel for two subsampled cases. The solid and dotted lines refer to a sample voxel size of 6.12 µm and 12.24 µm, respectively. The converged permeability is represented along the horizontal dashed line

Darcy for both the 6.12 and 12.24 µm voxel sizes. In the case of the 12.24 µm voxel size, a grid cell size of less than 7 µm appears to be sufficient.

Another approach is to consider the ratio of the number of grid cells per single voxel. While this does not account for the effect of pore throat size, at sufficiently high resolutions the pore space resolution effect may be negligible. Figure 7b shows the change in permeability as a function of the ratio of grid cells per voxel. The sample volume does not change across binning levels, so there are 256 voxels per side for the 6.12 µm voxel size case and 128 voxels per side for the 12.24 µm voxel size case. The permeability converges to the same value at a grid cell to voxel ratio of 2 for both cases, suggesting that at finer resolutions, the ratio of grid cells per voxel may also be used to determine an appropriate mesh size.

3.3 Workflow and Extension to Complex Geometries

A generalized summary of the workflow is given as follows:

1. Acquire single 3D tomographic scan of sample at a high resolution sufficient to clearly resolve pore space
2. Perform pixel binning to generate datasets at different lower resolutions
3. Segment pore volume from each dataset, either manually or with an automatic method (Otsu, watershed, etc.)
4. Calculate properties (ϕ, k, unconformity ratio, etc.) for each dataset
5. Determine error due to resolution effect for relevant properties; use to improve validation of values obtained from digital rock physics calculations

While the above methodology is simple, one can apply it easily to sandstone systems as shown in this work. Applications to more complex systems with less uniform pore size distributions or evidence of microporosity is ongoing and will require careful consideration of the potential limitations. Incorporating the microporosity may be done at the image acquisition stage through higher-resolution acquisitions, or modeling stage by extending the flow model using a Darcy–Brinkman approach (Soulaine et al. 2016). This methodology is also not limited to only micro-XRM 3D data, but can be used with nano-XRM or FIB-SEM acquired 3D data as well. Choosing the appropriate imaging tool requires knowing the pore size through MIP, gas sorption, or other direct pore characterization techniques.

4 Conclusion

The effect of image resolution on porosity and permeability was investigated for a sandstone pore network. By binning the original, high-resolution dataset by a factor of 2 multiple times, the change in error in porosity and permeability relative to the finest resolution was calculated from a numerical solver. The primary source of error is due to reassignment of voxels along the pore/solid interface and changes in pore connectivity as image resolution decreased. This methodology keeps the image processing and numerical setup steps simple and isolates the effect of image resolution and threshold choice on the rock connectivity and properties. Understanding how image quality affects the final rock properties provides a way to predict, from a single acquisition, the uncertainty involved when estimating porosity and permeability. Understanding this error helps improve the confidence in values obtained from DRP. This method can be generalized to study the effect of error in simple porous systems and future work involves extending this approach to dual porosity and other more complex systems.

Acknowledgements We thank the TOTAL STEMS project for financial support. We thank the Stanford Center for Computational Earth & Environmental Sciences for computational support. Part of this work was performed at SNSF on a ZEISS Xradia 520 Versa (NSF award CMMI-1532224). SNSF is supported by the NSF as part of the National Nanotechnology Coordinated Infrastructure under award ECCS-1542152.

References

Aljamaan, H., Alnoaimi, K., Kovscek, A.R.: In-depth experimental investigation of shale physical and transport properties. In: Unconventional Resources Technology Conference, Denver, Colorado pp. 1120–1129 (2013)

Andrä, H., Combaret, N., Dvorkin, J., et al.: Digital rock physics benchmarks-Part I: imaging and segmentation. Comput. Geosci. **50**, 25–32 (2013a)

Andrä, H., Combaret, N., Dvorkin, J., et al.: Digital rock physics benchmarks-part II: computing effective properties. Comput. Geosci. **50**, 33–43 (2013b)

Arganda-Carreras, I., Fernández-González, R., Muñoz-Barrutia, A., et al.: 3D reconstruction of histological sections: application to mammary gland tissue. Microsc. Res. Tech. **73**, 1019–1029 (2010)

Bazaikin, Y., Gurevich, B., Iglauer, S., et al.: Effect of CT image size and resolution on the accuracy of rock property estimates. J. Geophys. Res. Solid Earth **122**, 3635–3647 (2017)

Bear, J.: Dynamics of Fluids in Porous Media. Dover, Dover Civil and Mechanical Engineering Series 5. American Elsevier Publishing Company (1972)

Beckingham, L.E., Peters, C.A., Um, W., et al.: 2D and 3D imaging resolution trade-offs in quantifying pore throats for prediction of permeability. Adv. Water Resour. **62**, 1–12 (2013)

Berg, S., Saxena, N., Shaik, M., et al.: Generation of ground truth images to validate micro-CT image-processing pipelines. Lead. Edge **37**, 412–420 (2018)

Cnudde, V., Boone, M.N.: High-resolution X-ray computed tomography in geosciences: a review of the current technology and applications. Earth-Sci. Rev. **123**, 1–17 (2013)

Greenshields, C.J.: OpenFOAM User Guide Version 3.0.1. Tech. Rep. December (2015)

Guibert, R., Nazarova, M., Horgue, P., et al.: Computational permeability determination from pore-scale imaging: sample size, mesh and method sensitivities. Transp. Porous Med. **107**, 641–656 (2015)

Kaestner, A., Lehmann, E., Stampanoni, M.: Imaging and image processing in porous media research. Adv. Water Resour. **31**, 1174–1187 (2008)

Leu, L., Berg, S., Enzmann, F., et al.: Fast X-ray micro-tomography of multiphase flow in berea sandstone: a sensitivity study on image processing. Transp. Porous Med. **105**, 451–469 (2014)

Patankar, S.V.: Numerical heat transfer and fluid flow. Hemisphere Pub. Corp., Washington (1980)

Peng, S., Marone, F., Dultz, S.: Resolution effect in X-ray microcomputed tomography imaging and small pore's contribution to permeability for a Berea sandstone. J. Hydrol. **510**, 403–411 (2014)

Saxena, N., Hows, A., Hofmann, R., et al.: Imaging and computational considerations for image computed permeability: operating envelope of digital rock physics. Adv. Water Resour. **116**, 127–144 (2018)

Schlüter, S., Sheppard, A., Brown, K., et al.: Image processing of multiphase images obtained via X-ray microtomography: a review. Water Resour. Res. **50**, 3615–3639 (2014)

Schneider, C.A., Rasband, W.S., Eliceiri, K.W.: NIH Image to ImageJ: 25 years of image analysis. Nat. Methods **9**, 671–675 (2012)

Shah, S.M., Gray, F., Crawshaw, J.P., et al.: Micro-computed tomography pore-scale study of flow in porous media: effect of voxel resolution. Adv. Water Resour. **95**, 276–287 (2016)

Sheppard, A.P., Sok, R.M., Averdunk, H.: Techniques for image enhancement and segmentation of tomographic images of porous materials. Phys. A Stat. Mech. Appl. **339**, 145–151 (2004)

Soulaine, C., Gjetvaj, F., Garing, C., et al.: The impact of sub-resolution porosity of X-ray microtomography images on the permeability. Transp. Porous Med. **113**, 227–243 (2016)

Vega, B., Dutta, A., Kovscek, A.R.: CT imaging of low-permeability, dual-porosity systems using high x-ray contrast gas. Transp. Porous Med. **101**, 81–97 (2014)

Vinegar, H.J., Wellington, S.L.: Tomographic imaging of three-phase flow experiments. Rev. Sci. Instrum. **58**, 96–107 (1987)

Washburn, E.W.: The dynamics of capillary flow. Phys. Rev. **17**, 273–283 (1921)

Weller, H.G., Tabor, G., Jasak, H., et al.: A tensorial approach to computational continuum mechanics using object-oriented techniques. Comput. Phys. **12**, 620 (1998)

Whitaker, S.: Flow in porous media I: a theoretical derivation of Darcy's law. Transp. Porous Med. **1**, 3–25 (1986)

Wildenschild, D., Sheppard, A.P.: X-ray imaging and analysis techniques for quantifying pore-scale structure and processes in subsurface porous medium systems. Adv. Water Resour. **51**, 217–246 (2013)